# Laser-field-strength dependence of solid high-order harmonic generation from doped systems

Tian-Jiao Shao*

*School of Information Science and Engineering, NingboTech University, Ningbo 315100, China*
*and State Key Laboratory of Magnetic Resonance and Atomic and Molecular Physics, Wuhan Institute of Physics and Mathematics, Innovation Academy for Precision Measurement Science and Technology, Chinese Academy of Sciences, Wuhan 430071, China*

(Received 20 March 2023; revised 19 June 2023; accepted 19 July 2023; published 3 August 2023)

We have theoretically studied the field-strength-dependent high-order harmonic generation (HHG) from doped systems like nanosize or bulk materials. Our results show that when the amplitude of the vector potential $A_{\text{peak}}$ of the driving laser reaches the half-width of the Brillouin zone ($\pi/a_0$), the harmonic yield of the undoped systems is larger than that of the doped systems. The band-climbing process enhances the interband transition of HHG for higher conduction bands. We find that the donor-doped states and valence-band states from the doped system both contribute to the HHG. The destructive interference between the above two channels results in the harmonic yield from the undoped system overtaking that of the doped system when $A_{\text{peak}}$ is around or higher than $\pi/a_0$, especially when the phase of HHG contributed by the above two channels is close to $\pi$ rad. When $A_{\text{peak}}$ is below $\pi/a_0$, the harmonic yield of the doped systems is stronger than that of the undoped systems. The atomic doping density also influences the field-strength-dependent spectra.

DOI: 10.1103/PhysRevA.108.023105

## I. INTRODUCTION

With the development of ultrafast laser technology, high-order harmonic generation (HHG) in a gas medium was first observed experimentally in 1987 [1]. A three-step model was proposed to explain the physical mechanism of HHG in a gas [2,3]. Based on the HHG, isolated attosecond-pulse synthesis in experiments [4,5], the characterization of electronic structure, and ultrafast dynamics were realized [6–8]. With the development of midinfrared lasers [9,10], the experiment with HHG in solids was carried out and has become a research hot topic. The density and highly oriented arrangement of ions in solids cause the HHG in solids to have many differences from its counterpart in gases, such as the double-plateau structure of HHG spectra [11,12], the unique dependence on the ellipticity of the driving field [13–15], the linear dependence on the driving field strength [13,16,17], and so forth.

In addition, the electronic structure and band energies of solid targets can be designed through means of material-processing technology and can then be used to control the HHG process. Unlike gas media, solid target materials can be used for the following: growing nanostructures on the surface [18–20], modifications [21], reducing the dimension of a material [22–24], stacking [25], heterostructures [26], applying stress and strain [27–29], doping [30–39], and other material-engineering methods. These methods can change the electronic structure of the solid target, form the surface plasmon polaritons [18–20], and change the local solid medium and driving field [21], and then HHG can be enhanced.

The acceptor dopant will form an impurity energy level that is unoccupied in the band gap. Driven by the electric field, the electrons in the valence band (VB) of the acceptor-doped semiconductor are easier to excite to the impurity energy level, and more holes can be created in the VB than in the undoped system. However, for the donor-doped semiconductor, the electrons in the occupied impurity energy level are easier to excite to the conduction band (CB) compared with other states in the VB, and more electrons can be created in the CB compared than in the undoped semiconductor.

The physical scheme of the HHG in doped systems has been theoretically investigated [32–39]. The addition of the impurity energy level plays the role of a "ladder" for the optical transition from a band with lower energy to one with higher energy and greatly affects the HHG dynamics [32,34,38]. In 2017, Huang *et al.* theoretically found the second plateau of the HHG spectra of donor-doped semiconductors is enhanced compared with that of the undoped system by using the time-dependent Schrödinger equation (TDSE) method [32]. Their work indicated the narrower band gap and Brillouin zone in the donor-doped system strengthen the population in the CBs and improves the HHG emission. In 2018, Almalki *et al.* developed a microscopic three-step model for HHG from impurities [33]. In 2019, Yu *et al.* reported the enhancement of the HHG in the donor-doped semiconductor by using a time-dependent density-functional-theory (TDDFT) simulation. Their work showed that the atomiclike impurity state can be explained by a semiclassical three-step model [34]. In 2019, Jia *et al.* investigated the HHG magnetically doped topological insulator $Bi_2Se_3$ and found the crucial interplay between laser polarization and the symmetry of the material [35]. In 2020, Mrudul *et al.* investigated spin-polarized defects in two-dimensional hexagonal boron nitride by using TDDFT [36]. Their calculation revealed that different spin channels are influenced differently by the spin-polarized defect. In the same year, Pattanayak *et al.*'s work

*shaotj@nit.zju.edu.cn

 

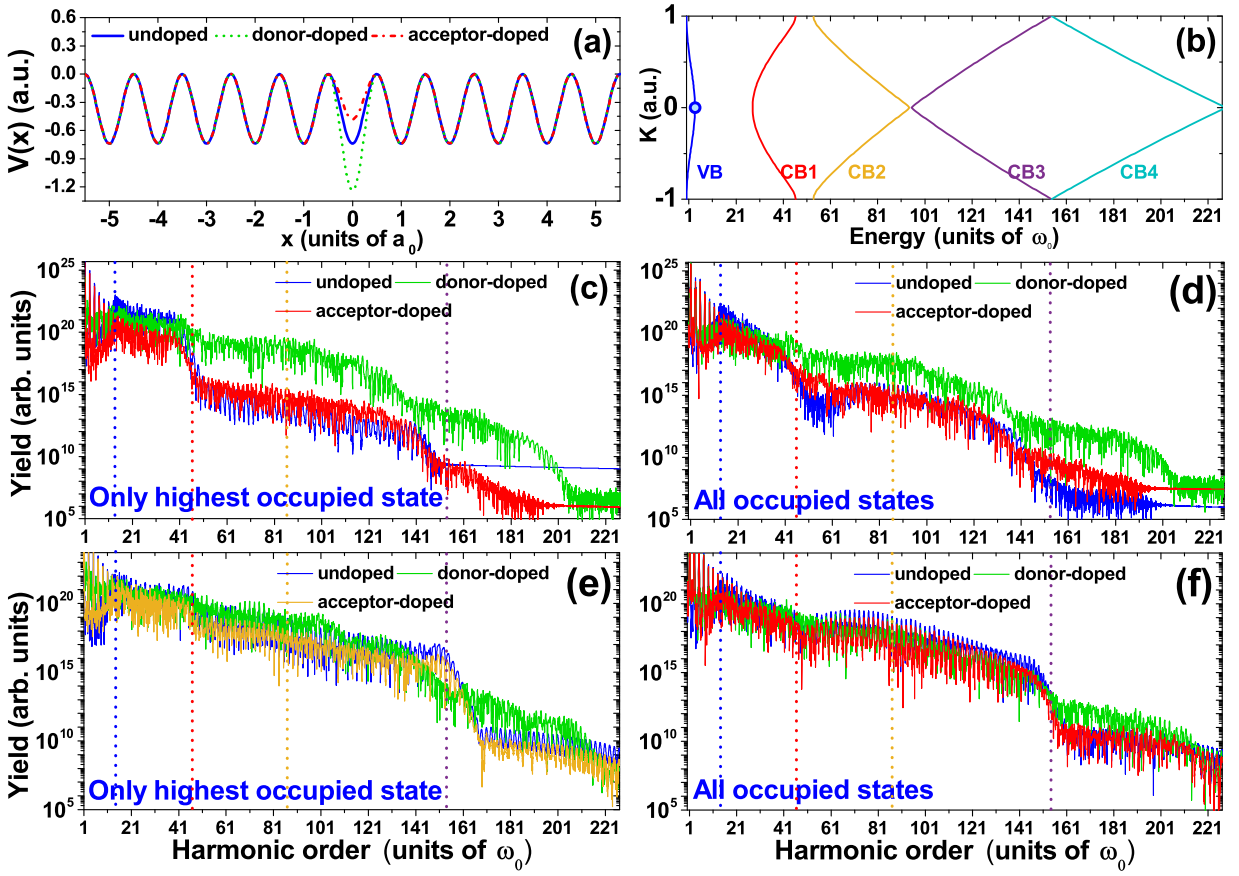


FIG. 1. (a) The blue solid line, green dashed line, and red dash-dotted line show the potential of the undoped, donor-doped, and acceptor-doped systems, respectively. (b) The band structure of the undoped system was calculated by using the Bloch-state expansion method. The blue scatter in the center of the VB is the highest occupied state for the undoped system which contributes more to the HHG than the other occupied states. (c) and (d) Comparison of the HHG spectra in the undoped, donor-doped, and acceptor-doped systems driven by an eight-cycle Gaussian laser pulse with field strength $E_0 = 0.0038$ a.u. and a central wavelength of 4000 nm. (e) and (f) Same as (c) and (d), except for the field strength is $E_0 = 0.0045$ a.u.

pointed out the impact of vacancy defects on the cutoff and yield of HHG [37]. In 2021, Zhao *et al.* investigated the influence of the donor- and acceptor-doped impurities on HHG and found that an impurity energy level in the middle of the band gap will lead to a higher yield of HHG emission [38]. In 2021, Nefedova *et al.* experimentally and numerically investigated the field-strength dependence of the HHG in Cr-doped MgO [30]. An enhancement of the HHG was found even though the defect concentration is low, which agrees with theoretical prediction [32,34,38]. In 2022, Yu *et al.* proposed a formula estimating the strength of the HHG spectrum from the impurity state which links to the tunneling Keldysh model [39].

In this work, the field-strength-dependent HHG from the doped systems is analyzed for a broad range of field strengths. We find that the enhancement of HHG in the donor-doped system is limited to a particular range of the field strength of the driving laser. The enhancement from doping is no longer preserved when the amplitude of the vector potential $A_{\text{peak}}$ is around or above the half-width $\pi/a_0$ of the Brillouin zone, with $a_0$ being the lattice constant.

## II. METHODS

The calculations in this work are based on the solution of the TDSE in the periodic potential [40–43]. The Mathieu-type potential is used to describe the periodic potential. For an undoped periodic lattice, the potential is given by $V(x) = -V_0[1 + \cos(2\pi x/a_0)]$, with $V_0 = 0.37$ a.u. and lattice constant $a_0 = 8$ a.u. Mathieu-type potentials are often used to simulate HHG in solids. The periodic potential of the undoped system is shown by the blue solid line in Fig. 1(a).

For the doped system, the case in which a dopant replaces the atoms of undoped systems is discussed in our work. The dopant does not change the lattice constant, and the potential energy of donor-doped and acceptor-doped semiconductors can be written as [32]

$$V(x) = \begin{cases} -V_0[1 + \cos(2\pi x/a_0)] & a \leqslant x \leqslant b \quad \text{or} \quad c \leqslant x \leqslant d, \\ -(V_0 + \Delta V)[1 + \cos(2\pi x/a_0)] & b < x < c, \end{cases} \tag{1}$$

where $\Delta V = -0.13$ for acceptor-doped semiconductors and $\Delta V = 0.25$ for donor-doped semiconductors. Because the dopant in the donor-doped system will contribute more electrons, the excess positive charge will deepen the potential energy. Thus, $\Delta V$ is positive for the donor-doped system and negative for the dopant in the acceptor-doped system.

The atomic doping density is defined as the ratio of the number of impurities to the total number of atoms. The typical atomic doping density of the bulk crystals in the experiment is between 0.1% and 3%. The band structure is not changed much at a low doping rate of around 1% [34]. In our work, an atomic doping density of 0.83% is used in Figs. 1–6. The HHG spectra for the doped system are calculated for one dopant atom in a finite chain with $N = 121$ ions. For $N = 121$ ions, the generated HHG spectra have all well-resolved structures compared with the HHG spectra from the bulk system [41,44,45]. To test the convergence of the results, the field-strength-dependent calculation for HHG spectra is also carried out for $N = 488$ and $N = 1220$ for comparison, and the results are presented in Appendix A.

In Fig. 7, HHG spectra in the doped system with different atomic doping densities of 1.64%, 2.44%, and 9.09% are compared. For doping densities of 1.64%, 2.44%, and 9.09%, the finite chain is constructed for 2 dopant atoms in a finite chain with $N = 122$ ions, 4 dopant atoms in a finite chain with $N = 124$ ions, 11 dopant atoms in a finite chain with $N = 121$ ions, respectively.

Figure 1(a) shows the potential energy of acceptor-doped (red dash-dotted line), undoped (blue solid line), and donor-doped (green dashed line) semiconductors, respectively. In Fig. 1(a), the eigenstate energy of the above atomic chain is obtained by solving the eigenstate wave function on a coordinate grid [32]. The band structure in $k$ space can be obtained by the method of Bloch-state expansion [40,41,43], as shown in Fig. 1(b). After the eigenstate is obtained, the time-dependent calculation with the external driving laser field is solved in coordinate space by using the second-order split-operator method [46]. After the time-dependent wave function $\psi_i(t)$ is obtained, the laser-induced current contributed by the $i$th occupied state can be obtained by evaluating the expectation value of the momentum operator, $j_i(t) = \langle\psi_i(t)|\hat{p}|\psi_i(t)\rangle$. The current including the contributions of all electrons can be expressed as

$$j(t) = -\sum_{i=1}^{N} \langle\psi_i(t)|\hat{p}|\psi_i(t)\rangle, \tag{2}$$

where $i$ is the eigenstate number and $N$ is the number of atoms. The corresponding HHG spectra contributed by the $i$th occupied state or all occupied states can be obtained by performing the Fourier transform of the corresponding current.

The driving laser field used in our work has a Gaussian profile in the time domain and is given by $E(t) = E_0 \exp[-4\ln(2)t^2/\tau^2]\cos(\omega_0 t)$, where $E_0$ is the amplitude of the driving field, $\omega_0$ is the fundamental frequency, and $\tau$ is the FWHM of the laser field; $\tau = 8$ o.c. (optical cycle) is applied in our calculations. The TDSEs are solved by the split-operator method with $2^{16} = 65\,536$ temporal grid points. The coordinate-space discretization is sampled with $2^{14} = 4096$ points in space. The maximum momentum cutoff is obtained with Nyquist's sampling theorem, $p_c = \frac{\pi}{\delta x} = 13.2893$ a.u.

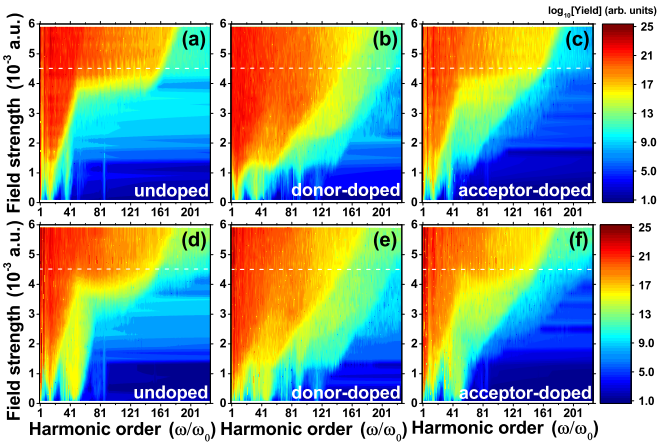


FIG. 2. False-color representations of the harmonic spectra varying with the field strength $E_0$ (in logarithmic scale). The white dashed line corresponds to the $E_0 = 0.0045$ a.u. (a) and (d) undoped system, (b) and (e) donor-doped system, and (c) and (f) acceptor-doped system. (a)–(c) The HHG spectra are obtained by Fourier transforming the current calculated by including only the highest occupied state. (d)–(f) The HHG spectra are obtained by Fourier transforming the current calculated by including all occupied states.

The vector potential of the driving laser field is defined as $A(t) = -\int_{-\infty}^{t} E(t')dt'$. Then the amplitude of the vector potential is given by $A_{\text{peak}} = E_0/\omega_0$. The wave vector of the electron is defined as [47,48]

$$k(t) = k_0 + \frac{e}{\hbar}A(t), \tag{3}$$

where $k_0$ is the initial wave vector at the $\Gamma$ point. When the electron-hole pairs are created through tunnel excitation, the excited carrier experiences intraband motion driven by the laser field. In the classical model, when an electron and a hole recombine, harmonic photons are emitted with an order given by $\eta(t) = \frac{\varepsilon_c(k(t)) - \varepsilon_v(k(t))}{\hbar\omega_0}$, where $\varepsilon_c(k(t))$ and $\varepsilon_v(k(t))$ are the energies of electrons in the CB and holes in the VB, respectively.

## III. RESULTS AND DISCUSSION

### A. Field-strength-dependent solid high-order harmonic generation

Figure 1(b) presents the energy band of the undoped system in $k$ space. In Fig. 1(b), the blue, red, orange, purple, and cyan solid lines show the VB, conduction band 1 (CB1), conduction band 2 (CB2), conduction band 3 (CB3), and conduction band 4 (CB4), respectively.

Figures 1(c) and 1(d) illustrate the HHG spectra driven by an eight-cycle Gaussian pulse with field strength $E_0 = 0.0038$ a.u. and a central wavelength of 4000 nm. The vertical blue, red, orange, and purple dashed lines in Figs. 1(c) and 1(f) denote the minimum band gap between CB1 and VB and the band gap energy between CB1 and the VB at the boundary of the Brillouin zone (BZ) which leads to the cutoff energy of the first plateau, the cutoff energy of the second plateau, and the cutoff energy of the third plateau, respectively.

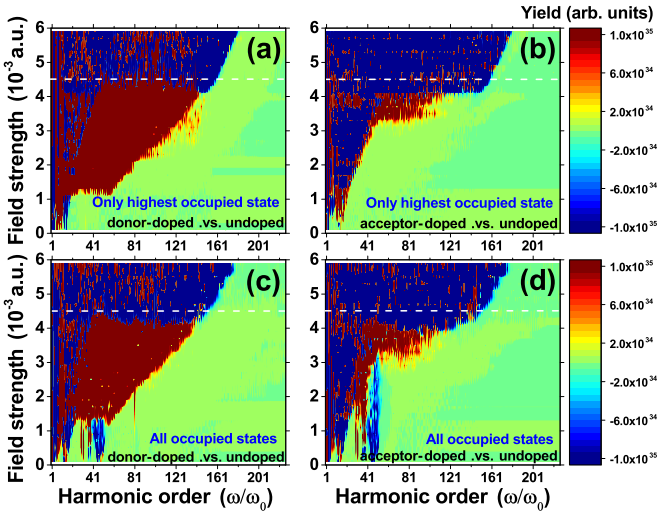


FIG. 3. Left: the HHG yield difference obtained by subtracting the yield of the undoped system from that of the donor-doped system. Right: the HHG yield difference obtained by subtracting the yield of the undoped system from that of the acceptor-doped system. The darkest red indicates HHG yield from the doped system is stronger than that of the undoped system. The darkest blue shows that the HHG yield from the undoped system is larger. (a) The difference between Figs. 2(b) and 2(a). (b) The difference between Figs. 2(c) and 2(a). (c) The difference between Figs. 2(e) and 2(d). (d) The difference between Figs. 2(f) and 2(d). The yield difference is plotted on a linear scale.

In Figs. 1(c) and 1(d), as in Huang *et al.*'s work [32], the second plateau of the HHG spectra from the donor-doped semiconductor (green solid line) is enhanced by several orders compared with its counterparts from the acceptor-doped and undoped systems. The results that include only the highest occupied state and all electrons show the same trend. However, the HHG spectra from acceptor-doped semiconductors are slightly stronger than those of undoped semiconductors. The large enhancement of the HHG spectra from donor-doped semiconductors agrees with Yu *et al.*'s work using the TDDFT calculation [34] and the experimental observation of enhancement of HHG spectra in Cr-doped MgO [30].

In Figs. 1(e) and 1(f), the HHG spectra are driven by the same Gaussian laser field as Figs. 1(c) and 1(d) but have a larger field strength, $E_0 = 0.0045$ a.u. This field strength corresponds to $A_{\text{peak}} = \pi/a_0$, which is equal to the half-width of the Brillouin zone. In this case, the magnitude of the vector potential is able to drive the electron to reach the boundary of the BZ. Different from the case of $E_0 = 0.0038$ a.u., the yield of HHG spectra in the undoped system is larger than in the acceptor-doped and donor-doped systems.

Figure 2 illustrates that the HHG spectra vary with the field strength of the driving field. The HHG spectra shown in Figs. 2(a)–2(c) are calculated while including only the highest occupied state. However, Figs. 2(d)–2(f) present the results calculated while including all the occupied states. The white dashed line marks the driving field strength $E_0 = 0.0045$ a.u., which corresponds to $A_{\text{peak}} = \pi/a_0$.

In Figs. 2(a) and 2(d), when $E_0 = 0.0045$ a.u., the HHG spectra from undoped semiconductors shows a double-plateau structure [49]. For $A_{\text{peak}} = \pi/a_0$, the wave vector of the electron $k(t) = k_0 + A(t)$ can reach the boundary of the BZ. The electrons in CB1 can be pumped to CB2 through the band-climbing mechanism [49], and then the electrons experience intraband motion driven by the laser field. In the following half optical cycle, the electrons are driven backward and move toward the center of the BZ ($k = 0$) and can be pumped to CB3 through band climbing. Therefore, the second plateau and higher plateau structure appear when $A_{\text{peak}} = a_0/\omega_0$.

However, in Figs. 2(b) and 2(e), for the donor-doped system, when the $A_{\text{peak}}$ is still below $a_0/\omega_0$, the second plateau and higher-order emission are clearly observed. The doped impurity energy level between the VB and CB1 is not occupied by electrons. Compared with the occupied states in the VB, the impurity energy level is closer to CB1 and is easier to excite to CB1. The ladder provided by the impurity energy level increases the excitation rates of optical transition and strengthens the HHG dynamics [34,38].

Figures 2(c) and 2(f) present the field-strength dependence of HHG spectra in acceptor-doped semiconductors. Like in the donor-doped system in the middle column, when $A_{\text{peak}}$ is still below $a_0/\omega_0$, the second plateau and higher-order emission are observed. However, in acceptor-doped semiconductors, the impurity energy level between the VB and CB1 is occupied by the electrons, but the impurity energy level is close to the VB. Compared with the undoped semiconductor, the electrons in the VB are easier to excite to CB1 with the same electric-field strength. This makes the yield of HHG spectra stronger than that of the undoped system when the amplitude of the vector potential is below $a_0/\omega_0$. However, because the doped energy level in the acceptor-doped system is not occupied by the electrons, the acceptor-doped semiconductor does not have a channel of HHG contributed by the excitation from the impurity energy level to CB1 directly. This causes the yield of HHG from the acceptor-doped system to be less efficient than that of the donor-doped system.

In Fig. 3, the effect of doping on HHG is investigated by subtracting the yield of HHG spectra in the undoped system from that of the doped system. Figures 3(a) and 3(c) show the difference between the HHG spectra from the donor-doped and undoped systems. Figures 3(b) and 3(d) present the difference between the HHG spectra from the acceptor-doped and undoped systems. The darkest red indicates that the yield in the doped system is higher than in the undoped system, while the darkest blue indicates that the yield in the undoped system is higher than in the doped system. Both the calculation including only the highest occupied state and that including all occupied states show that the division separated by the white-dashed line corresponds to a field strength of $E_0 = 0.0045$ a.u. ($A_{\text{peak}} = a_0/\omega_0$). When $A_{\text{peak}}$ is below $a_0/\omega_0$, the HHG from the doped system is stronger. In contrast, when $A_{\text{peak}}$ is around or above $a_0/\omega_0$, the HHG from the undoped system is brighter. This result indicates that the enhancement of the yield in HHG from doping is field strength dependent for a typical atomic doping density of around 1% in the experiment.

In Fig. 4, the temporal profile of HHG is calculated by including all occupied states. Figures 4(a)–4(c) present the HHG driven by an eight-cycle, 4000-nm laser with field strength $E_0 = 0.0038$ a.u. from the undoped, donor-doped, and acceptor-doped systems, respectively. In Fig. 4(b), the

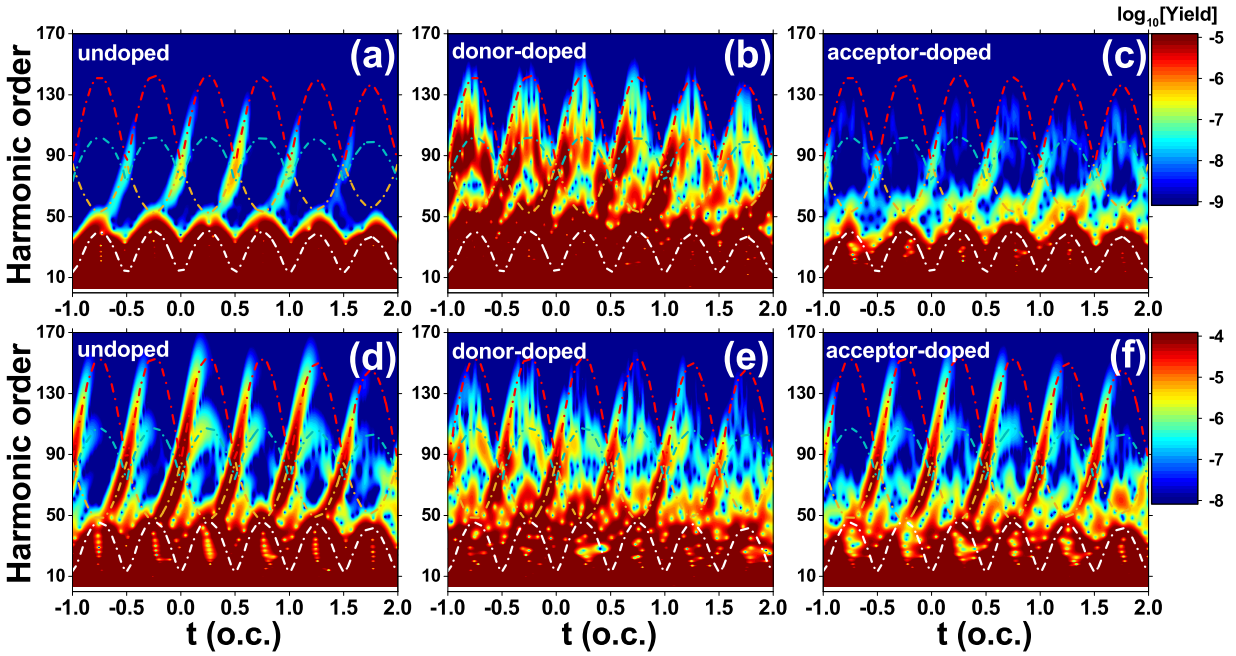


FIG. 4. The temporal profile of HHG spectra plotted on a logarithmic scale. (a)–(c) The temporal profile of HHG driven by a laser field with $E_0 = 0.0038$ a.u. (d)–(f) The temporal profile of HHG driven by a laser field with $E_0 = 0.0045$ a.u. (a) and (d) Undoped system, (b) and (e) donor-doped system, and (c) and (f) acceptor-doped system. The white, orange, and red dash-dotted lines show the trajectory predicted by the quasiclassical model for the interband transition from conduction bands CB1, CB2, and CB3 to the VB, respectively. The cyan dash-dotted lines represent the trajectory involving the transition between CB3 and CB1. When the driving field strength $E_0 = 0.0038$ a.u., the harmonic yields at the second and third plateaus of the donor-doped semiconductor become much stronger than those of the undoped target and acceptor-doped system. For higher field strength ($E_0 = 0.0045$ a.u.), for the doped target, the harmonic in the second and third plateaus become weaker than in the undoped system.

trajectory of the donor-doped systems is stronger than those of the undoped and acceptor-doped systems in Figs. 4(a) and 4(c), respectively.

In Figs. 4(d)–4(f), for a driving field strength of $E_0 = 0.0045$ a.u., the temporal profile of HHG in the undoped semiconductor in Fig. 4(d) is stronger than those of the donor-doped and acceptor-doped systems in Figs. 4(e) and 4(f), respectively. In addition, the HHG trajectories in Fig. 4(d) are almost perfectly repeated in each half optical cycle and have a well-resolved temporal structure. This indicates that these trajectories will interfere with each other constructively, which leads to the enhancement of the total HHG spectra in the frequency domain.

In Fig. 5, the left, middle, and right columns show the band structures of the undoped, donor-doped, and acceptor-doped systems, respectively. The top row presents the eigenstate energies in ascending order, including the energy bands of the VB, CB1, CB2, CB3, and all doped impurity energy levels. The "in-band" energies in Figs. 5(b) and 5(c) for the donor-doped system are almost unchanged compared with those of the undoped system shown in Fig. 5(a) [34]. In Fig. 5(b), for the donor-doped system, the impurity energy level between the VB and CB1 is occupied by electrons. However, for the acceptor-doped system in Fig. 5(c), the impurity energy level between the VB and CB1 is unoccupied.

Figures 5(d)–5(f) are a pictorial representation of the band structure and laser-field-induced electron trajectories of the undoped, donor-doped, and acceptor-doped systems in $k$ space, respectively. For the donor-doped system in Fig. 5(e),

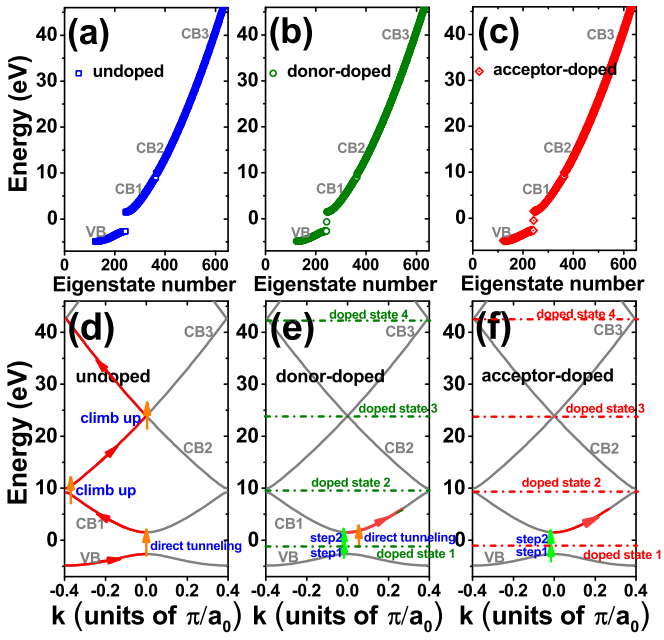


FIG. 5. The energy band structure of the (a) and (d) undoped, (b) and (e) donor-doped, and (c) and (f) acceptor-doped systems, including valence band VB1 and conduction bands CB1, CB2, and CB3 and all doped energy levels. (a)–(c) The band energies are plotted in ascending order. (d)–(f) Pictorial representation of the band structure and electron trajectories in momentum space.

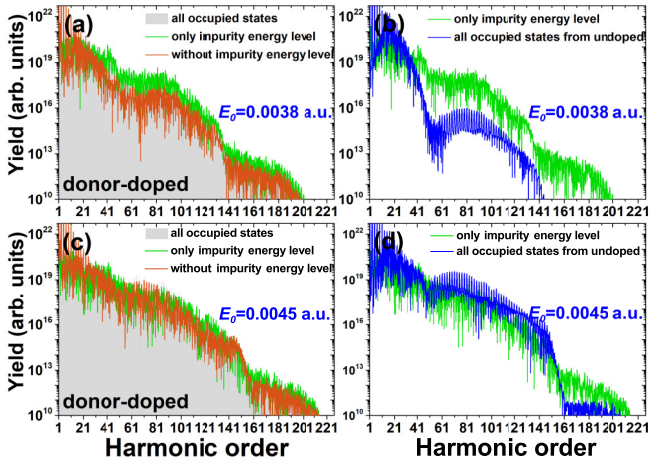


FIG. 6. The HHG spectra for the donor-doped system driven by a laser with (a) field strength $E_0 = 0.0038$ a.u. and (c) $E_0 = 0.0045$ a.u.. The gray shading, orange solid line, and green solid line represent HHG obtained by Fourier transforming the total current from all occupied states, with only the highest doped-energy-level state, and without this state, respectively. A comparison of the HHG spectra contributed by the doped energy level, with (b) field strength of the driving field $E_0 = 0.0038$ a.u. and (d) $E_0 = 0.0045$ a.u.

the electrons can be directly pumped from the occupied impurity energy level to CB1, which is marked by the upward orange arrow between the VB and CB1 in Fig. 5(e). According to the Keldysh model [50], the excitation rate increases exponentially with the narrowing of the band gap. The occupied doped energy level which is closer to CB1 has a much larger excitation rate to reach CB1 compared with the other occupied states in the VB.

When the field strength of the driving field is weak ($A_{\text{peak}} < a_0/\omega_0$), for the donor-doped system, the direct excitation from the impurity energy level is the main factor which causes the several-order enhancement of the HHG dynamics. For the acceptor-doped system in Fig. 5(f), the unoccupied impurity states between the VB and CB1 provide a ladder in the step-by-step transition process which results in an increase of HHG.

The orange arrows between CB1 and CB2 in Fig. 5(d) denote the "band-climbing" process [49]. When the field strength of the driving laser is large ($A_{\text{peak}} > \pi/a_0$), after the transition to CB1 from the VB, the electrons experience intraband motion driven by the laser, can be accelerated to the BZ boundary, and can climb up to the higher CB2. In the following half optical cycle, the electrons pumped to CB2 are driven backward by the laser field and experience intraband motion along CB2. When the electrons in CB2 are driven to the vicinity of $k = 0$, the electrons can climb to CB3. The band-climbing process was proposed to explain the multiplateau structure in HHG spectra from solids [49]. In our work, when $A_{\text{peak}} = \pi/a_0$, the electrons in the undoped semiconductor can be pumped to CB2 and then CB3 through a band-climbing process, which leads to a large enhancement of the yield in the second and third plateaus on HHG the spectra.

In Fig. 6, we analyze the HHG spectra contributed by the doped impurity energy level. The left column of Fig. 6 presents the HHG spectra from the donor-doped system. The

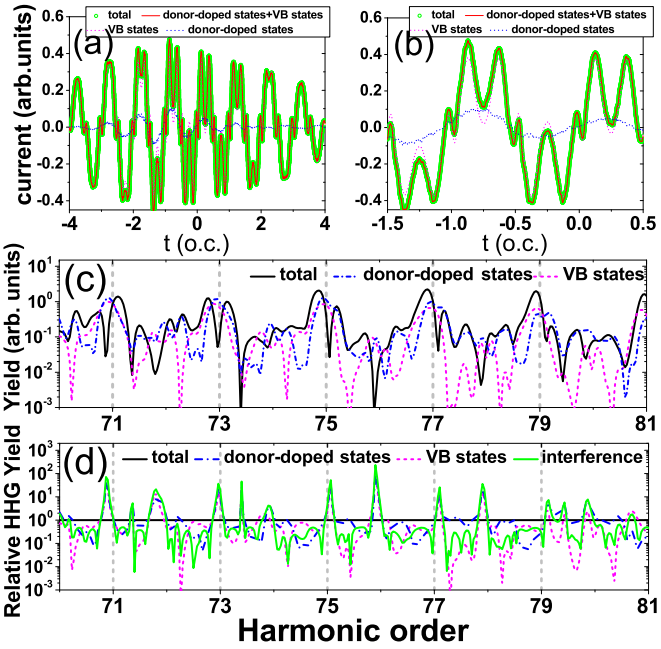


FIG. 7. The laser-induced current and HHG spectra in the donor-doped system when $E_0 = 0.0045$ a.u. (a) Total (green circles), donor-doped-state HHG (blue dash-dotted line), VB-state HHG (magenta dashed line), and the coherent superposition of donor-doped-state and VB-state HHG (red solid line). (b) Detailed view of (a). (c) Donor-doped-state HHG (blue dash-dotted line), VB-state HHG (magenta dashed line), and the total HHG (black solid line). (d) Yields of donor-doped-state HHG (blue dash-dotted line), VB-state HHG (magenta dashed line), the absolute value of the interference $|S_{\text{interference}}|$ (green solid line), and their coherent sum (black solid line) relative to the total harmonic yield.

right column of Fig. 6 compares the HHG spectra from the impurity energy level in the donor-doped system and HHG spectra from the undoped system by including all occupied states.

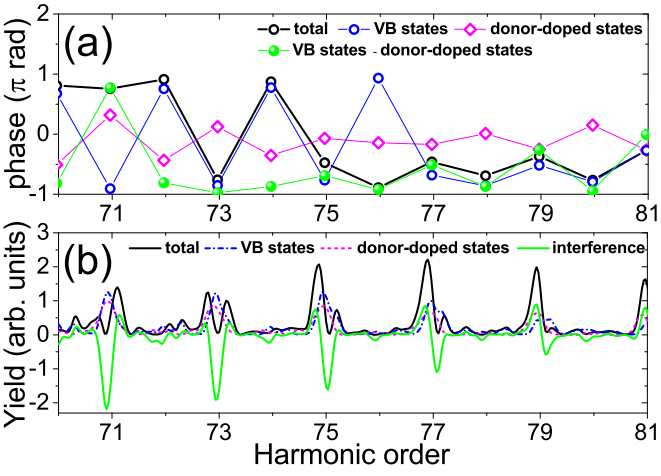


FIG. 8. Phase of the HHG spectra. (a) HHG spectra in the frequency range of $70\omega_0$–$81\omega_0$. (b) The interference term (green solid line) is plotted to reveal the emergence of the destructive interference between the donor-doped-state HHG and VB-state HHG.

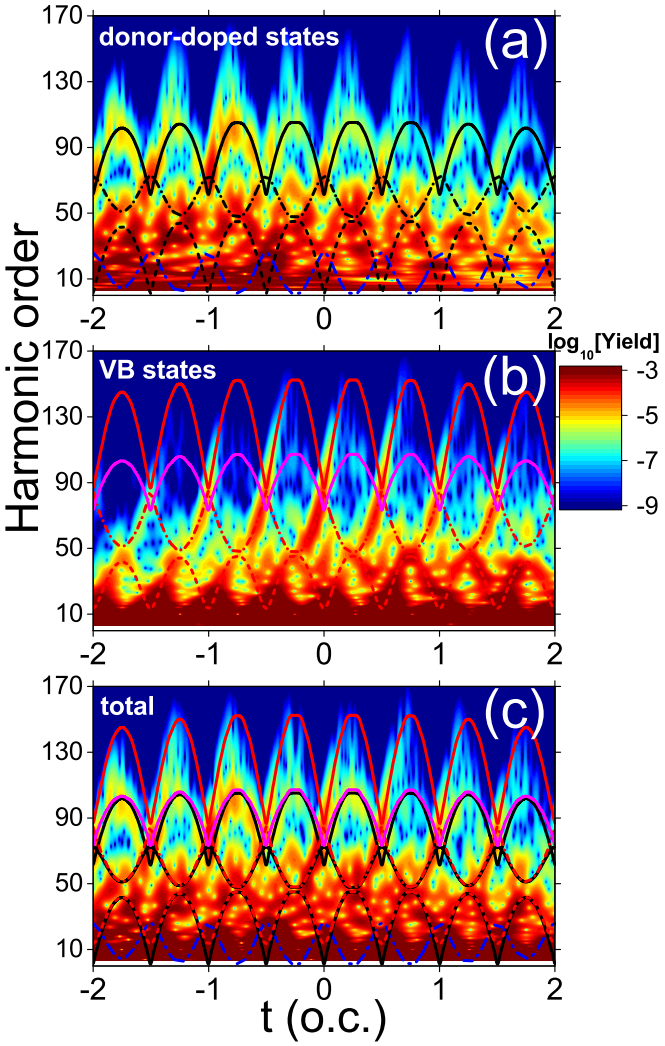


FIG. 9. Time-frequency analysis of the HHG in donor-doped HHG for $E_0 = 0.0045$ a.u. (a) Temporal profile of the donor-doped-state HHG. The black solid line, black dash-dotted line, black dashed line, and blue dash-dotted line show the quasiclassical analysis of the transition from donor-doped state 4 to CB2, donor-doped state 3 to CB1, donor-doped state 3 to CB2, and donor-doped state 2 to CB1, respectively. (b) The temporal profile of the VB-state HHG. The red solid line, red dash-dotted line, and red dashed line show the trajectory predicted by the quasiclassical model for the interband transition from conduction bands CB3, CB2, and CB1 to the VB, respectively. The magenta solid line shows the interband transition from CB3 to CB1. (c) Temporal profile of the total HHG.

In Figs. 6(a) and 6(c), the gray shading represents the HHG spectra contributed by all occupied states. The green solid line and orange solid line represent the HHG spectra contributed by only the impurity energy level and the other occupied states, respectively. In Fig. 6(a), for driving field strength $E_0 = 0.0038$ a.u., in a wide range of orders, the HHG spectra obtained from the highest occupied state agree with the spectra including all occupied states. This agrees with Yu *et al.*'s work [34], in which HHG spectra from the donor-doped system are mainly contributed by the impurity energy level.

In Fig. 6(b), HHG spectra contributed by only the impurity energy level are larger than the HHG spectra from the undoped system including all electrons. This indicates that the enhancement of the yield of HHG by donor doping is mainly caused by the impurity energy level.

In Fig. 6(c), driven by a laser with field strength $E_0 = 0.0045$ a.u., the yield of the HHG spectra contributed by all the other states is comparable to the HHG contributed by only the impurity energy level. As discussed above, when the amplitude of the vector potential reaches $a_0/\omega_0$, a large number of electrons can be driven to the vicinity of the boundary of the BZ and pumped to CB2 through band climbing.

In Fig. 6(d), the HHG spectra from the undoped system are stronger than the HHG spectra contributed by the impurity energy level from the donor-doped system. In addition, the HHG spectra from the undoped system have a clear harmonic signal of integer order. This indicates that the HHG trajectories in the time domain constructively interfere with each other.

### B. Analysis of the doped states, valence-band states, and interference contributions to the harmonic spectrum

In this work, the total current is obtained as

$$j_{\text{total}}(t) = -\langle\psi(t)|\hat{p}|\psi(t)\rangle, \tag{4}$$

where $\psi(t)$ is the time-dependent wave function numerically solved by the TDSE and $\hat{p}$ is the momentum operator. We calculate the time-dependent donor-doped states $\psi_{\text{donor}}(t)$ and valence-band states $\psi_{\text{vb}}(t)$ using TDSE and extract the currents contributed by the donor-doped states and valence-band states as follows:

$$j_{\text{donor}}(t) = -\sum_{n\in n_{\text{donor}}} \langle\psi_{\text{donor}}(t)|\hat{p}|\psi_{\text{donor}}(t)\rangle, \tag{5}$$

$$j_{\text{vb}}(t) = -\sum_{n\in n_{\text{vb}}} \langle\psi_{\text{vb}}(t)|\hat{p}|\psi_{\text{vb}}(t)\rangle, \tag{6}$$

where the superscripts donor and vb are the indices for eigenstates. Then,

$$j_{\text{total}}(t) = j_{\text{donor}}(t) + j_{\text{vb}}(t). \tag{7}$$

The harmonic spectra are obtained from the Fourier transform of the temporal currents [42]:

$$S_{\text{total}}(\omega) = \left|\int j_{\text{total}}(t) e^{-i\omega t} dt\right|^2, \tag{8}$$

$$S_{\text{total}}(\omega) = S_{\text{donor}}(\omega) + S_{\text{vb}}(\omega) + S_{\text{inteference}}(\omega), \tag{9}$$

where

$$S_{\text{donor}}(\omega) = \left|\int j_{\text{donor}}(t) e^{-i\omega t} dt\right|^2, \tag{10}$$

$$S_{\text{vb}}(\omega) = \left|\int j_{\text{vb}}(t) e^{-i\omega t} dt\right|^2, \tag{11}$$

and

$$\begin{aligned} &S_{\text{interference}}(\omega) \\ &= \int j^*_{\text{donor}}(t)\exp(i\omega t)dt \int j_{\text{vb}}(t)\exp(-i\omega t)dt \\ &\quad + \int j^*_{\text{vb}}(t)\exp(i\omega t)dt \int j_{\text{donor}}(t)\exp(-i\omega t)dt \end{aligned} \tag{12}$$

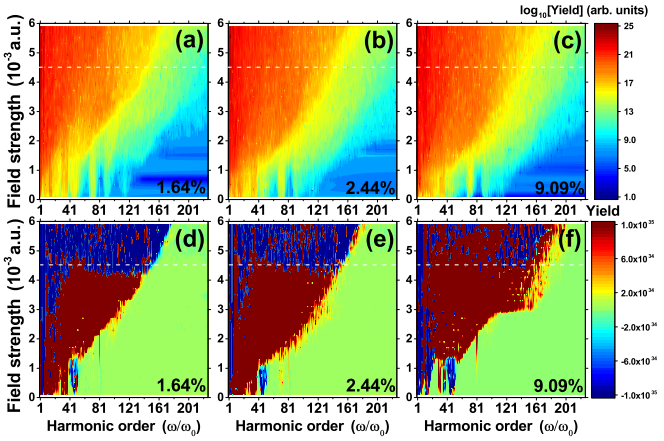


FIG. 10. False-color representations of the harmonic spectra varying with the field strength $E_0$ for doping rates of (a) 1.64%, (b) 2.44%, and (c) 9.09%. The HHG spectra are obtained by Fourier transforming the current calculated with all occupied states. The white dashed line corresponds to $E_0 = 0.0045$ a.u. (d)–(f) The difference between HHG yields from the donor-doped and undoped systems. The laser parameters are the same as those used in Fig. 4.

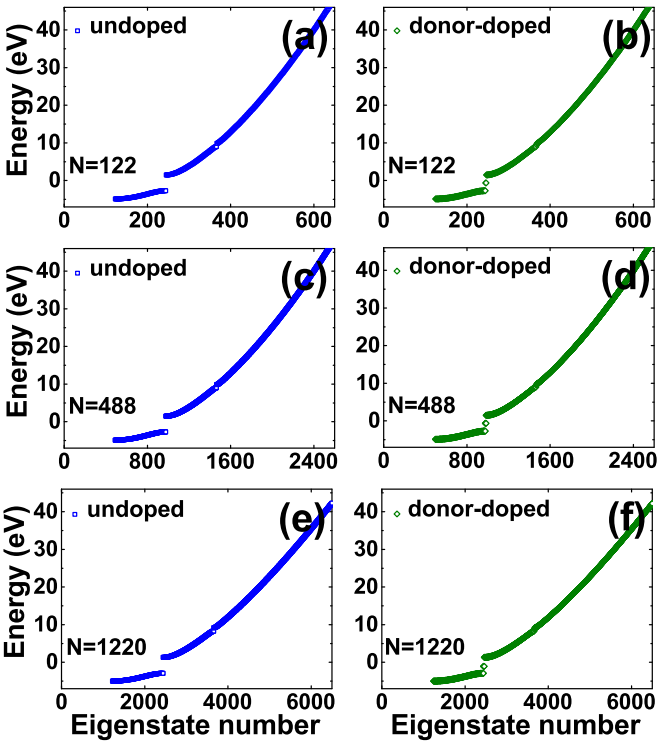


FIG. 11. The energy-band structures of the (a), (c), and (e) undoped and (b), (d), and (f) donor-doped systems, including valence band VB1 and conduction bands CB1, and CB2, CB3 and all impurity energy levels. The band energies are plotted in ascending order. System sizes of $N = 122$, 488, and 1220 are presented with growing system sizes from top to bottom.

are donor-doped states, VB states, and interference contributions to the spectra, respectively.

The laser-induced current is shown in Fig. 7(a). The amplitude of the current contributed by the donor-doped state (magenta dashed line) is close to that contributed by the valence-band states (blue dash-dotted line). The superposition of donor-doped-state current and VB current $[j_{\text{donor}}(t) + j_{\text{vb}}(t)]$ is completely consistent with the total current $j_{\text{total}}(t)$. The current over a short time period is presented in Fig. 7(b) to show the details of Fig. 7(a).

In Figs. 7(c) and 7(d), the total, donor-doped-state, valence -band-state, and interference spectra are calculated independently according to Eqs. (8)–(12). The summation of donor-doped-state and VB-state spectra cannot explain the final structure. Since the yields of donor-doped-state and VB-state spectra are close, their interference will have a significant impact on the total spectra.

The yields of donor-doped states (magenta dashed line), VB states (blue dash-dotted line), and the interference harmonic (green solid line) relative to the total harmonic yield are shown in Fig. 7(d). Near orders 70–80, there is a suppression of the total harmonic caused by destructive interference.

Figure 8(a) shows the extracted phases of donor-doped-state (magenta scatters) and VB-state (blue scatters) HHG spectra. Phase differences between donor-doped states and VB states for orders 70–76 are about $-\pi$ rad where destructive interference occurs. The interference between the donor-doped states and VB states was discussed less in previous work.

In Fig. 8(b), the spectrum is displayed on a linear scale, and the interference term has negative values. For harmonic orders 71, 73, 75, and 77, the interference counteracts the contributions from donor-doped states and VB states, and the total yield is suppressed.

Figures 9(a)–9(c) show the small-window time-frequency analysis of donor-doped states, VB states, and total current. In Fig. 9(a), the energy difference between the CBs and VB is plotted, corresponding to the laser-induced quasiclassical trajectory. Figure 9(b) presents the energy difference between the donor-doped states and CBs and the energy difference between the donor-doped states and the VB. The temporal profile of the total HHG in Fig. 9(c) comes from the coherent superposition of donor-doped-state HHG and VB-state HHG. Figure 9(a) shows that the transition between the donor-doped states and the energy bands covers the energy of the entire platform region in the HHG spectra. This fact indicates that the instant intensity of the total harmonic is affected by the interference between the donor-doped states and VB states.

### C. Field-strength-dependent solid high-order harmonic generation for other doping rates

Further, the effect of atomic doping density on the HHG spectra is investigated. Figures 10(a)–10(c) represent the HHG from the donor-doped semiconductor with atomic doping densities of 1.64%, 2.44%, and 9.09%, respectively. Figures 10(d)–10(f) represent the difference between the HHG spectra from the donor-doped system and those from the undoped system. With the increase of the atomic doping density, the channels transited directly from the occupied impurity energy level to CB1 will increase, which will give rise to the enhancement of the HHG.

In Fig. 10(d), when the atomic doping density is equal to 1.64%, the enhancement of the HHG by doping shows clear

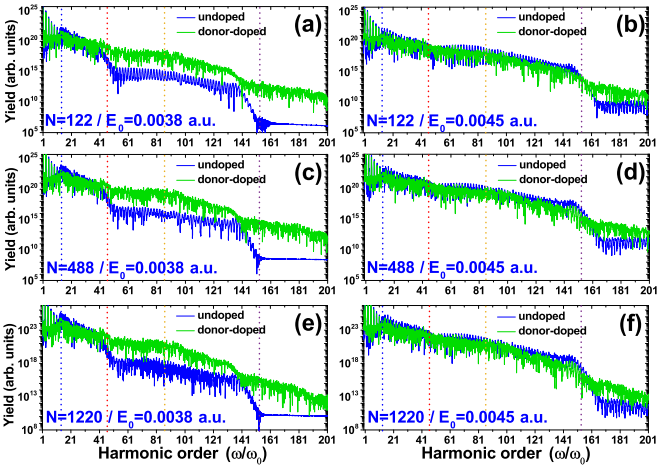


FIG. 12. HHG spectra for system sizes of $N = 122$, 488, and 1220 using the same laser parameters as in Fig. 1. The HHG spectra are presented with growing system size from top to bottom to test the convergence of our calculation results. The vertical blue, red, orange, and purple dashed lines present the minimum band gap between CB1 and the VB and the band-gap energy between CB1 and the VB at the boundary of the BZ which leads to the cutoff energy of the first plateau, the cutoff energy of the second plateau, and the cutoff energy of the third plateau, respectively. In the left column, when the amplitude of the vector potential $A_{\text{peak}}$ is below $\pi/a_0$ ($E_0 = 0.0038$ a.u.), the yield of HHG from the donor-doped system is several orders larger than that of the undoped system. In the right column, when $A_{\text{peak}}$ reaches the half-width of the BZ ($E_0 = 0.0045$ a.u.), on the contrary, the yield of HHG from the undoped system is larger than that of the donor-doped system. Since the excitation for crystal-momentum states far from the minimal band gap is low, the total HHG spectra include the crystal-momentum states that are located within a distance of 5% from the minimum band gap.

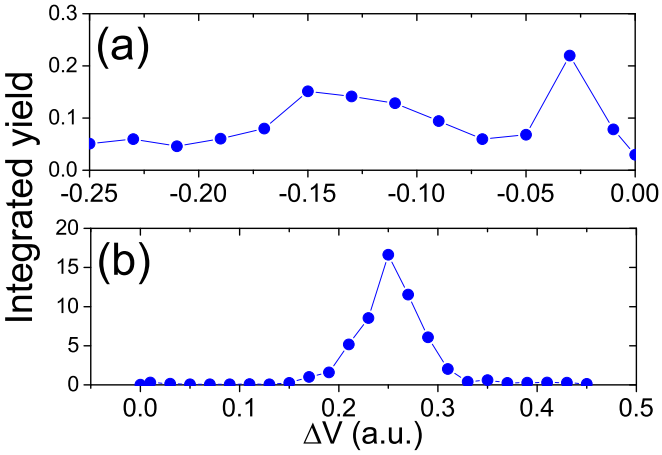


FIG. 13. Integrated HHG yields of the second plateau vary with doping potential depth $\Delta V$. (a) The acceptor-doped system with negative $\Delta V$. (b) The donor-doped system with positive $\Delta V$. Maximal yields of HHG are located around $\Delta V = 0.25$ for the donor-doped system.

dependence on the laser field strength. An atomic doping density of 1.64% should be common in experiments. When the atomic doping density increases to 2.44% and 9.09%, with the increase in impurity energy levels, for $A_{\text{peak}}$ greater than $\pi/a_0$, the advantage of an undoped system become less obvious. However, such a high doping density of 9.09% is rare in typical experiments.

## IV. CONCLUSION

In conclusion, our research showed that under the common atomic doping density of 0.1%–3%, the improvement in the harmonic yield in doped systems such as nanomaterials and bulk materials is field strength dependent. When the amplitude of the driving laser vector potential $A_{\text{peak}}$ is lower than $\pi/a_0$, because the impurity energy level provides a ladder for interband transition, electrons more easily transit from the VB to CB1, CB2, and CB3, which causes the harmonic yields of the acceptor-doped and donor-doped systems to be larger than that of the undoped system. In particular, in a donor-doped system, the electrons from impurity energy levels can be directly excited to CB1, which greatly improves the harmonic yield.

When $A_{\text{peak}}$ is around $\pi/a_0$ or higher than $\pi/a_0$, because the electrons in CB1 can move to the boundary of the BZ, the electrons can climb up to CB2 and then experience intraband motion in CB2 driven by the external field and can then be pumped to the higher CB3 through band climbing near $k = 0$, which greatly enhances the interband transition [49]. The time-frequency analysis in Fig. 4 indicates that the instant intensity in a half-cycle HHG process from the undoped system is stronger than that in the doped system. This indicates that the result of the harmonic yield from the undoped system overtaking that of the doped system when $A_{\text{peak}}$ is around or higher than $\pi/a_0$ is not because of the interference over the cycles.

For the HHG from the doped system, the donor-doped states and VB states both contribute to the HHG. The destructive interference between the above two channels results in the harmonic yield from the undoped system overtaking that of the doped system when $A_{\text{peak}}$ is around or higher than $\pi/a_0$. In Figs. 7–9, the HHGs contributed by the donor-doped states and VB states were calculated separately. The harmonic phases contributed by the donor-doped states and the VB states are different, resulting in destructive interference. The destructive interference counteracts contributions from the donor-doped states and the VB states, especially when the phase of HHG contributed by the above two channels is close to $\pi$ rad.

The effect of atomic doping density on HHG spectra was further investigated. With the increase of atomic doping density, the yield of HHG from the doped system can be increased further, which will reduce this field-strength dependence.

## ACKNOWLEDGMENTS

I thank Prof. X.-B. Bian, T.-Y. Du, and J.-Q. Liu for discussions. I am grateful for the support from the National Natural Science Foundation of China (Grant No. 12104395), the Zhejiang Provincial Natural Science Foundation of China (Grant No. LQ22A040004), and the Ningbo Natural Science Foundation (Project No. 2023J289).

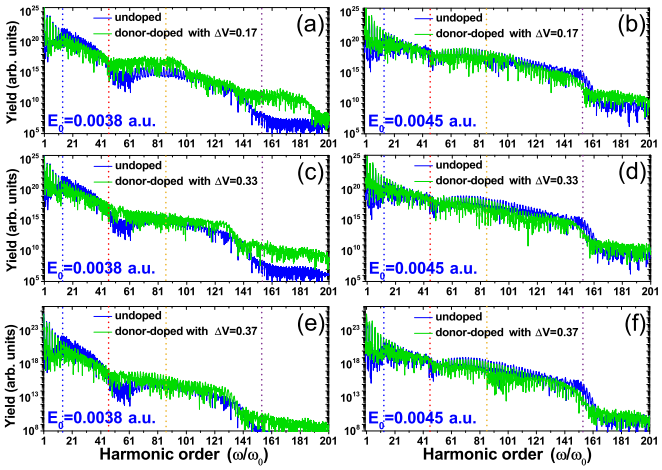


FIG. 14. Comparison of HHG spectra between the undoped system (blue solid line) and the donor-doped system (green solid line) with other doping parameters $\Delta V = 0.17$, 0.33, and 0.37 using the same laser parameters as in Fig. 1. The vertical blue, red, orange, and purple dashed lines present the minimum band gap between CB1 and the VB and the band-gap energy between CB1 and the VB at the boundary of the BZ which leads to the cutoff energy of the first plateau, the cutoff energy of the second plateau, and the cutoff energy of the third plateau, respectively. In the left column, the amplitude of the vector potential $A_{\text{peak}}$ is below $\pi/a_0$ ($E_0 = 0.0038$ a.u.). In the right column, $A_{\text{peak}}$ reaches the half-width of the BZ ($E_0 = 0.0045$ a.u.).

## APPENDIX A: CONVERGENCE TESTS

Figures 11 and 12 present the convergence test of our calculation results. Figure 11 shows the energy band structures of the undoped [Figs. 11(a), 11(c) and 11(e)] and donor-doped [Fig. 11(b), 11(d) and 11(f)] systems of a finite chain in ascending order. For doping densities of 1.64%, finite chains with system sizes of $N = 122$, $N = 488$, and $N = 1220$ ions are constructed for 2, 8, and 20 dopant atoms, respectively.

For instance, in Fig. 11(a), for the undoped system with a system size of $N = 122$, the VB, CB1, CB2, and CB3 correspond to state numbers 123–244, 245–366, 367–488, and 489–610, respectively. In Fig. 11(b), for the donor-doped system with a system size of $N = 122$, the VB, CB1, CB2, and CB3 correspond to state numbers 125–244, 247–366, 369–488, and 491–610, respectively. State numbers 245 and 246 correspond to the occupied impurity energy states between the VB and CB1. Figures 11(c) and 11(d) present the band energies of undoped and donor-doped systems with system sizes of $N = 488$, respectively. Figures 11(e) and 11(f) have system sizes of $N = 1220$.

Figure 12 shows a comparison of HHG spectra from undoped and donor-doped systems for system sizes of $N = 122$ [Figs. 12(a) and 12(b)], 488 [Figs. 12(c) and 12(d)], and 1220 [Figs. 12(e) and 12(f)] using the same laser parameters as in Fig. 1. The HHG spectra are presented with increasing system size from top to bottom to test the convergence of our calculation results. Since the excitation for crystal-momentum states far from the minimal band gap is low, the total HHG spectra in Fig. 12 include the crystal-momentum states that are located within a distance of 5% from the minimum band gap. For system sizes $N = 122$ [Figs. 12(a) and 12(b)], $N = 488$ [Figs. 12(c) and 12(d)], and $N = 1220$ [Figs. 12(e) and 12(f)], we observe nearly identical HHG spectra. In the left column, when the amplitude of the vector potential $A_{\text{peak}}$ is below $\pi/a_0$ ($E_0 = 0.0038$ a.u.), the yield of HHG from the donor-doped system is several orders larger than that of the undoped system. In the right column, when $A_{\text{peak}}$ reaches the half-width of the BZ ($E_0 = 0.0045$ a.u.), on the contrary, the yield of HHG from the undoped system is larger than the donor-doped one. Our results show, using the conventional doping ratio of 0.5%–3%, the enhancement of HHG by doping is field strength dependent in doped systems such as nanosized and bulk materials.

## APPENDIX B: OTHER DOPING PARAMETERS

As shown in Figs. 13(a) and 13(b), the yield of the second plateau modulates with the doping parameter $\Delta V$. The maximal integrated yield of HHG is located near $\Delta V = 0.25$ in the donor-doped system. This is the reason for $\Delta V = -0.13$ being adopted for the acceptor-doped system and $\Delta V = 0.25$ being adopted for the donor-doped system [38]. Thus, the maximal HHG yields can be achieved in the doped system.

Other doping parameters $\Delta V = 0.17$, 0.33, and 0.37 are calculated in Fig. 14. The donor-doped system reveals a higher intensity than the undoped system for almost all harmonic orders for driving field strength $E_0$ below 0.0038 a.u. Above $E_0 = 0.0045$ a.u., in Figs. 14(b), 14(d), and 14(f), the undoped system intensity dominates in the second plateau region.

[1] A. McPherson, G. Gibson, H. Jara, U. Johann, T. S. Luk, I. McIntyre, K. Boyer, and C. K. Rhodes, Studies of multiphoton production of vacuum-ultraviolet radiation in the rare gases, J. Opt. Soc. Am. B **4**, 595 (1987).

[2] P. B. Corkum, Plasma Perspective on Strong Field Multiphoton Ionization, Phys. Rev. Lett. **71**, 1994 (1993).

[3] M. Lewenstein, Ph. Balcou, M. Y. Ivanov, A. L'Huillier, and P. B. Corkum, Theory of high-harmonic generation by low-frequency laser fields, Phys. Rev. A **49**, 2117 (1994).

[4] P.-M. Paul, E. S. Toma, P. Breger, G. Mullot, F. Augé, P. Balcou, H. G. Muller, and P. Agostini, Observation of a train of attosecond pulses from high harmonic generation, Science **292**, 1689 (2001).

[5] M. Hentschel, R. Kienberger, C. Spielmann, G. A. Reider, N. Milosevic, T. Brabec, P. Corkum, U. Heinzmann, M. Drescher, and F. Krausz, Attosecond metrology, Nature (London) **414**, 509 (2001).

[6] M. Lein, J. P. Marangos, and P. L. Knight, Electron diffraction in above-threshold ionization of molecules, Phys. Rev. A **66**, 051404(R) (2002).

[7] J. Itatani, J. Levesque, D. Zeidler, H. Niikura, H. Pépin, J.-C. Kieffer, P. B. Corkum, and D. M. Villeneuve, Tomographic

imaging of molecular orbitals, Nature (London) **432**, 867 (2004).

[8] X.-B. Bian and A. D. Bandrauk, Probing Nuclear Motion by Frequency Modulation of Molecular High-Order Harmonic Generation, Phys. Rev. Lett. **113**, 193901 (2014).

[9] A. Dubietis, G. Jonušauskas, and A. Piskarskas, Powerful femtosecond pulse generation by chirped and stretched pulse parametric amplification in BBO crystal, Opt. Commun. **88**, 437 (1992).

[10] N. Ishii, K. Kaneshima, K. Kitano, T. Kanai, S. Watanabe, and J. Itatani, Carrier-envelope phase-dependent high harmonic generation in the water window using few-cycle infrared pulses, Nat. Commun. **5**, 3331 (2014).

[11] G. Ndabashimiye, S. Ghimire, M. Wu, D. A. Browne, K. J. Schafer, M. B. Gaarde, and D. A. Reis, Solid-state harmonics beyond the atomic limit, Nature (London) **534**, 520 (2016).

[12] Y. S. You, M. Wu, Y. Yin, A. Chew, X. Ren, S. Gholam-Mirzaei, D. A. Browne, M. Chini, Z. Chang, K. J. Schafer, M. B. Gaarde, and S. Ghimire, Laser waveform control of extreme ultraviolet high harmonics from solids, Opt. Lett. **42**, 1816 (2017).

[13] S. Ghimire, A. D. DiChiara, E. Sistrunk, P. Agostini, L. F. DiMauro, and D. A. Reis, Observation of high-order harmonic generation in a bulk crystal, Nat. Phys. **7**, 138 (2011).

[14] N. Yoshikawa, T. Tamaya, and K. Tanaka, High-harmonic generation in graphene enhanced by elliptically polarized light excitation, Science **356**, 736 (2017).

[15] N. Tancogne-Dejean, O. D. Mücke, F. X. Kärtner, and A. Rubio, Ellipticity dependence of high-harmonic generation in solids originating from coupled intraband and interband dynamics, Nat. Commun. **8**, 745 (2017).

[16] G. Vampa, C. R. McDonald, G. Orlando, D. D. Klug, P. B. Corkum, and T. Brabec, Theoretical Analysis of High-Harmonic Generation in Solids, Phys. Rev. Lett. **113**, 073901 (2014).

[17] G. Vampa, C. R. McDonald, G. Orlando, P. B. Corkum, and T. Brabec, Semiclassical analysis of high harmonic generation in bulk crystals, Phys. Rev. B **91**, 064302 (2015).

[18] S. Han, H. Kim, Y. W. Kim, Y.-J. Kim, S. Kim, I.-Y. Park, and S.-W. Kim, High-harmonic generation by field enhanced femtosecond pulses in metal-sapphire nanostructure, Nat. Commun. **7**, 13105 (2016).

[19] G. Vampa, B. G. Ghamsari, S. Siadat Mousavi, T. J. Hammond, A. Olivieri, E. Lisicka-Skrek, A. Yu Naumov, D. M. Villeneuve, A. Staudte, P. Berini, and P. B. Corkum, Plasmon-enhanced high-harmonic generation from silicon, Nat. Phys. **13**, 659 (2017).

[20] H. Liu, C. Guo, G. Vampa, J. L. Zhang, T. Sarmiento, M. Xiao, P. H. Bucksbaum, J. Vučković, S. Fan, and D. A. Reis, Enhanced high-harmonic generation from an all-dielectric metasurface, Nat. Phys. **14**, 1006 (2018).

[21] M. Sivis, M. Taucer, G. Vampa, K. Johnston, A. Staudte, A. Y. Naumov, D. Villeneuve, C. Ropers, and P. Corkum, Tailored semiconductors for high-harmonic optoelectronics, Science **357**, 303 (2017).

[22] Z. Lou, Y. Zheng, C. Liu, L. Zhang, X. Ge, Y. Li, J. Wang, Z. Zeng, R. Li, and Z. Xu, Ellipticity dependence of nonperturbative harmonic generation in few-layer $MoS_2$, Opt. Commun. **469**, 125769 (2020).

[23] H. Liu, Y. Li, Y. S. You, S. Ghimire, T. F. Heinz, and D. A. Reis, High-harmonic generation from an atomically thin semiconductor, Nat. Phys. **13**, 262 (2017).

[24] C. R. McDonald, K. S. Amin, S. Aalmalki, and T. Brabec, Enhancing High Harmonic Output in Solids through Quantum Confinement, Phys. Rev. Lett. **119**, 183902 (2017).

[25] G. Le Breton, A. Rubio, and N. Tancogne-Dejean, High-harmonic generation from few-layer hexagonal boron nitride: Evolution from monolayer to bulk response, Phys. Rev. B **98**, 165308 (2018).

[26] I. Alonso Calafell, L. A. Rozema, D. Alcaraz Iranzo, A. Trenti, P. K. Jenke, J. D. Cox, A. Kumar, H. Bieliaiev, S. Nanot, C. Peng *et al.*, Giant enhancement of third-harmonic generation in graphene–metal heterostructures, Nat. Nanotechnol. **16**, 318 (2021).

[27] R. Qin and Z.-Y. Chen, Strain-controlled high harmonic generation with Dirac fermions in silicene, Nanoscale **10**, 22593 (2018).

[28] T.-J. Shao, Y. Xu, X.-H. Huang, and X.-B. Bian, Strain effects on high-order harmonic generation in solids, Phys. Rev. A **99**, 013432 (2019).

[29] T. Tamaya, H. Akiyama, and T. Kato, Shear-strain controlled high-harmonic generation in graphene, Phys. Rev. B **107**, L081405 (2023).

[30] V. E. Nefedova, S. Fröhlich, F. Navarrete, N. Tancogne-Dejean, D. Franz, A. Hamdou, S. Kaassamani, D. Gauthier, R. Nicolas, G. Jargot, M. Hanna, P. Georges, M. F. Ciappina, U. Thumm, W. Boutu, and H. Merdji, Enhanced extreme ultraviolet high-harmonic generation from chromium-doped magnesium oxide, Appl. Phys. Lett. **118**, 201103 (2021).

[31] Z. Wang, H. Park, Y. H. Lai, J. Xu, C. I. Blaga, F. Yang, P. Agostini, and L. F. DiMauro, The roles of photo-carrier doping and driving wavelength in high harmonic generation from a semiconductor, Nat. Commun. **8**, 1686 (2017).

[32] T. Huang, X. Zhu, L. Li, X. Liu, P. Lan, and P. Lu, High-order-harmonic generation of a doped semiconductor, Phys. Rev. A **96**, 043425 (2017).

[33] S. Almalki, A. M. Parks, G. Bart, P. B. Corkum, T. Brabec, and C. R. McDonald, High harmonic generation tomography of impurities in solids: Conceptual analysis, Phys. Rev. B **98**, 144307 (2018).

[34] C. Yu, K. K. Hansen, and L. B. Madsen, Enhanced high-order harmonic generation in donor-doped band-gap materials, Phys. Rev. A **99**, 013435 (2019).

[35] L. Jia, Z. Zhang, D. Z. Yang, M. S. Si, G. P. Zhang, and Y. S. Liu, High harmonic generation in magnetically-doped topological insulators, Phys. Rev. B **100**, 125144 (2019).

[36] M. Mrudul, N. Tancogne-Dejean, A. Rubio, and G. Dixit, High-harmonic generation from spin-polarised defects in solids, npj Comput. Mater. **6**, 10 (2020).

[37] A. Pattanayak, M. M. S., and G. Dixit, Influence of vacancy defects in solid high-order harmonic generation, Phys. Rev. A **101**, 013404 (2020).

[38] Y.-P. Zhao, G. Wang, S.-J. Ding, and T.-Y. Du, Impact of donor and acceptor dopants in high-harmonic generation spectra of solids, J. Opt. Soc. Am. B **38**, 2223 (2021).

[39] C. Yu, U. Saalmann, and J. M. Rost, Enhanced high-order harmonics through periodicity breaks: From backscattering to impurity states, Phys. Rev. A **106**, 013105 (2022).

[40] M. Wu, S. Ghimire, D. A. Reis, K. J. Schafer, and M. B. Gaarde, High-harmonic generation from Bloch electrons in solids, Phys. Rev. A **91**, 043839 (2015).

[41] Z. Guan, X.-X. Zhou, and X.-B. Bian, High-order-harmonic generation from periodic potentials driven by few-cycle laser pulses, Phys. Rev. A **93**, 033852 (2016).

[42] X.-Q. Wang, Y. Xu, X.-H. Huang, and X.-B. Bian, Interference between inter- and intraband currents in high-order harmonic generation in solids, Phys. Rev. A **98**, 023427 (2018).

[43] X.-Q. Wang and X.-B. Bian, Model-potential method for high-order harmonic generation in monolayer graphene, Phys. Rev. A **103**, 053106 (2021).

[44] K. K. Hansen, D. Bauer, and L. B. Madsen, Finite-system effects on high-order harmonic generation: From atoms to solids, Phys. Rev. A **97**, 043424 (2018).

[45] K. K. Hansen, T. Deffge, and D. Bauer, High-order harmonic generation in solid slabs beyond the single-active-electron approximation, Phys. Rev. A **96**, 053418 (2017).

[46] M. D. Feit, J. A. Fleck, and A. Steiger, Solution of the Schrödinger equation by a spectral method, J. Comput. Phys. **47**, 412 (1982).

[47] T.-Y. Du and X.-B. Bian, Quasi-classical analysis of the dynamics of the high-order harmonic generation from solids, Opt. Express **25**, 151 (2017).

[48] G.-R. Jia, X.-H. Huang, and X.-B. Bian, Nonadiabatic redshifts in high-order harmonic generation from solids, Opt. Express **25**, 23654 (2017).

[49] T. Ikemachi, Y. Shinohara, T. Sato, J. Yumoto, M. Kuwata-Gonokami, and K. L. Ishikawa, Trajectory analysis of high-order-harmonic generation from periodic crystals, Phys. Rev. A **95**, 043416 (2017).

[50] L. V. Keldysh, Ionization in the field of a strong electromagnetic wave, J. Exp. Theor. Phys. **47**, 1945 (1964) [Sov. Phys. JETP **20**, 1307 (1965)].

# Web of Science™ Core Collection

**经检索《Web of Science™ Core Collection》，下述论文被《SCI - Expanded》收录。（数据获取：2023年09月05日）**

**标题:**Laser-field-strength dependence of solid high-order harmonic generation from doped systems

**作者:**Shao, TJ(Shao, Tianjiao)

**来源出版物:**PHYSICAL REVIEW A **卷:**108 **期:**2 **文献号:**023105

**出版时间:**2023,AUG 3 **DOI:**10.1103/PhysRevA.108.023105

**出版商:**AMER PHYSICAL SOC **出版商地址:**ONE PHYSICS ELLIPSE, COLLEGE PK, MD 20740-3844 USA

**文献类型:**Article **语种:**English

**入藏号:**WOS:001052958100003 **IDS号:**P8EW6

**地址:**[Shao, Tian-Jiao] NingboTech Univ, Sch Informat Sci & Engn, Ningbo 315100, Peoples R China; [Shao, Tian-Jiao] Chinese Acad Sci, Wuhan Inst Phys & Math, Innovat Acad Precis Measurement Sci & Technol, State Key Lab Magnet Resonance & Atom & Mol Phys, Wuhan 430071, Peoples R China

**通讯作者:**Shao, TJ (通讯作者)，NingboTech Univ, Sch Informat Sci & Engn, Ningbo 315100, Peoples R China.; Shao, TJ (通讯作者)，Chinese Acad Sci, Wuhan Inst Phys & Math, Innovat Acad Precis Measurement Sci & Technol, State Key Lab Magnet Resonance & Atom & Mol Phys, Wuhan 430071, Peoples R China.

**电子邮件:**shaotj@nit.zju.edu.cn

**ISSN:**2469-9926 **电子ISSN:**2469-9934

**ISO 来源文献缩写:**Phys. Rev. A **来源出版物页码计数:**12

**注:**

**以上检索结果均得到被检索人的确认。**本证明编号：NBT-SCIE-2023-6098

《SCI - Expanded》检索结果（收录情况）

浙大宁波理工学院图书馆

检索人(签名):

审核人(签章):

2023年09月11日

InCites™ Journal Citation Reports®

**经检索《Web of Science™》的JCR数据库，期刊《PHYSICAL REVIEW A》2022年JCR的影响因子情况：**

**ISSN：2469-9926**

**eISSN：2469-9934**

**2022年影响因子：2.900**

**PHYSICS, ATOMIC, MOLECULAR & CHEMICAL：Q2**

**OPTICS：Q2**

注：

1.以上检索结果均得到被检索人的确认。证明编号：NBT-SCIE-2023-6098-IF2022

2.论文的期刊影响因子应与该论文所发表期刊的年份相对应。

3.因JCR的最新数据截至到2022年，2023年出版论文的期刊影响因子以2022年的期刊影响因子为参考。

《JOURNAL CITATION REPORTS（JCR）》检索结果

浙大宁波理工学院图书馆

检索人(签名)

审核人(签章)

2023年09月11日